POLITECNICO DI TORINO
Repository ISTITUZIONALE

A computational framework for large-scale seismic simulations of residential building stock

(Article begins on next page)

22 September 2024

1   **A computational framework for large-scale seismic simulations of**

2   **residential building stock**

3   Sebastiano Marasco [1], Ali Zamani Noori [2], Marco Domaneschi[3], and Gian Paolo Cimellaro [4]*

4

5   **ABSTRACT**

6   Urban areas reveal particularly vulnerable due to the high concentration of people and, in many

7   cases, their hazard-prone location. Indeed, according to data from the United Nations, about 2/3

8   of the population will live in large cities by 2050, and the majority of the world's cities are

9   highly exposed to disasters. This paper presents a computational framework to assess the seismic

10   vulnerability and the damage of residential building portfolio in urban areas. First, a surrogated

11   model is proposed to estimate the global capacity of building structures. Monte Carlo simulations

12   are implemented to take into account the uncertainties associated with the material, mechanical,

13   and geometrical parameters. The proposed approach is validated through nonlinear finite element

14   models and a real case study. Then, the proposed computational framework is implemented and

15   applied to a virtual city that is envisioned for being representative of a typical Italian residential

16   building stock. The main achievement of this work is to introduce a new simplified approach for

17   large scale structural analyses to limit the computational efforts while providing reasonable

18   results.

19   **Keywords**: Simulation; Earthquake; Urban area; Capacity curve; Damage assessment.

20

[1]*Postdoctoral research associate, Department of Structural, Geotechnical and Building Engineering, Politecnico di Torino, Italy, E-mail: sebastiano.marasco@polito.it.*

[2]*Postdoctoral research associate, Department of Structural, Geotechnical and Building Engineering, Politecnico di Torino, Italy, E-mail: ali.zamani@polito.it.*

[3]*Assistant Professor, Department of Structural, Geotechnical and Building Engineering, Politecnico di Torino, Italy, E-mail: marco.domaneschi@polito.it.*

[4]* Corresponding author: Visiting Professor, Department of Structural & Environmental Engineering, University of California, Berkeley, Berkeley, USA, E-mail: gianpaolo.cimellaro@polito.it.*

1. INTRODUCTION

Recent disasters have shown the vulnerability of the built environment at the urban scale and how complex the process to improve its resilience is [1-6]. Earthquake response prediction of buildings portfolio requires the use of large-scale simulation methods which are based on statistical and deterministic approaches. In the first case, the building damage assessment is based on statistical data collected from previous seismic events [7]. One widely used method is the Damage Probability Matrix (DPM) which predicts the level of damage for different seismic intensities and buildings typologies [8]. The concept of DPM was widely adopted into the ATC-13 report [9] to evaluate the earthquake damage data for California that includes the DPMs for 78 different facility types. Later, Dolce, Kappos [10] applied a modified version of it to the city of Potenza (Southern Italy), while Eleftheriadou and Karabinis [11] extended the DPM-based methodology to the building stock in Southern Europe.

On the contrary, deterministic methods are usually based on physical models using nonlinear static or dynamic analyses. The former case may consider the Capacity Spectrum Method, CSM [12], or N2 method [13]. E.g., El Ezz, Nollet [14] adopted the CSM to assess the seismic damage of Quebec City, Canada.

Focusing on dynamic approaches, Korkmaz [15] proposed a probabilistic seismic safety assessment performing nonlinear analyses on unreinforced masonry low-rise buildings specific to Pakistan building portfolio. Furthermore, Tang, Lu [16] assessed the collapse resistance of Reinforced Concrete (RC) frame structures representative of the Chinese school stock using Incremental Dynamic Analysis (IDA) [17]. Xu, Lu [18] proposed a high-fidelity structural model to predict the seismic damage on buildings in urban areas. In the context of regional seismic damage simulation, Lu and Guan [19] proposed a shear model for Multi Degree of Freedom (MDOF) systems and a shear-flexure model for tall buildings.

45 The available large-scale simulation models assess the structural seismic damage and

46 vulnerability classifying the buildings into different groups (typological approach). Usually,

47 buildings are grouped based on building archetype, number of stories, seismic design level. For

48 example, the Global Earthquake Model (GEM) [20, 21] consists of an initiative to calculate and

49 communicate earthquake risk worldwide. One of its main components is the development of

50 open-source software for seismic hazard and risk assessment. The vulnerability model is based

51 on a fragility function for each building class contained in the exposure model.

52 Another example of a typological approach was implemented in the WP4 of the RISK-UE

53 project [22], which aims at developing vulnerability and fragility models for the current building

54 stock prevailing the European built environment. The main issues consist of classifying the

55 current building stock, implementing a first level (LM1) approach to assess the vulnerability, and

56 developing a second level (LM2) method to model the building capacity and fragility. The LM1

57 model is based on the definition of the building vulnerability through qualitative damage

58 matrices associated with the European Macroseismic Scale [23]. On the other hand, the LM2

59 method focuses on the quantification of the potential damage experienced by buildings after a

60 given ground shaking. Capacity models are developed for each building class to represent the

61 first mode response based on certain engineering parameters that characterize the nonlinear

62 structural behavior, while capacity curves are idealized as a bilinear function defined by the yield

63 and ultimate control points. The values of shear force and top displacement are determined in the

64 first period of vibration, design strength, overstrength, and ductility parameters. They are

65 identified by code requirements, experimental and empirical evidences, and expert evaluation.

66 The seismic performance of each building class is then evaluated by applying the CSM.

67   Although these approaches provide a rapid and simplified estimate, their results could be not

68   always equivalent to the actual response of the individual building. Indeed, it depends

69   significantly on the number of the involved parameters such as geometry, structural

70   characteristics, materials, etc. On the contrary, refined models allow a better estimation of the

71   seismic response of the individual building but require a large amount of data making the

72   simulation process computationally complex. E.g., Hori, Ichimura [24] developed a project to

73   study the earthquake effects in the urban environment using an Integrated Earthquake Simulation

74   (IES). The input data was collected into a Geographic Information System (GIS) and then

75   converted into suitable numerical models. Examples of applications of IES for Tokyo and

76   Istanbul are presented in [25, 26].

77   This paper proposes a surrogated nonlinear physical model that aims to be at an intermediate

78   level between a detailed description of the built environment, e.g. the IES project [24], and a

79   typological one [18, 20]. The new surrogated model is an equivalent Single Degree of Freedom

80   (SDOF) system used to reproduce the global seismic behavior of each residential building. It

81   allows limiting the computational efforts to a refined finite element (FE) model while predicting

82   the seismic response of an individual building more accurately than an approach based on

83   building classes.

84   The next section of the paper provides a detailed description of the capacity model of buildings.

85   The third section illustrates the damage assessment through nonlinear time history analysis. The

86   fourth section deals with the validation of the whole proposed computational framework. A real

87   case study is then considered to validate the proposed approach. Finally, in the last section, a

88   large-scale urban simulation is implemented.

2. BUILDING MODELLING

A new surrogated SDOF model is herein proposed to simulate the seismic response and assess the damage experienced by buildings during a seismic event (Fig. 1a). A backbone curve is implemented as representative of the global capacity of an individual building, whereas the strength degradation is accounted through a hysteresis model (Fig. 1b).
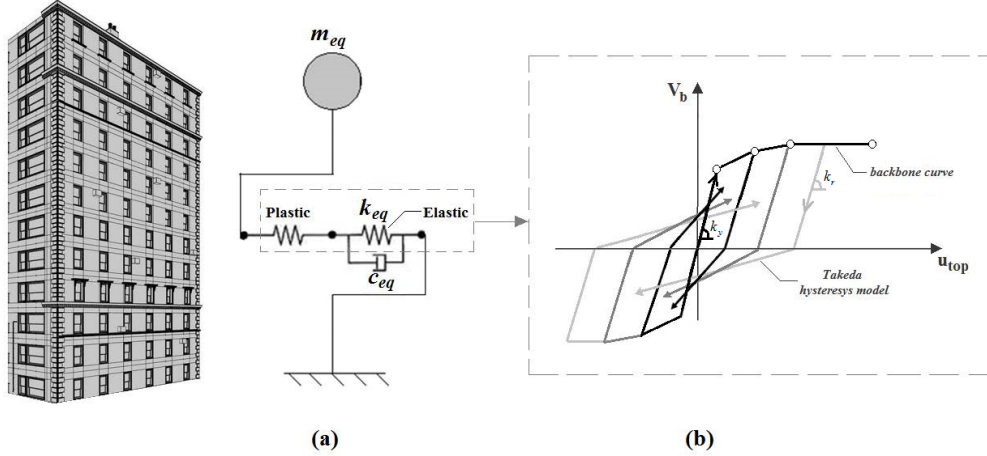

(a)   (b)

Fig. 1. Proposed surrogated SDOF model (a) and hysteresis model used to simulate the global dynamic buildings' behavior of RC buildings

The surrogated model adopts as response parameters the roof displacement at the center of mass [13] and the base shear [27]. The SDOF stiffness is characterized by the equivalent initial elastic stiffness k_{eq} [28] following by the post-elastic behavior. This last is assessed through the application of the kinematic theorem of limit analysis by considering different possible collapse mechanisms. The equivalent mass m_{eq} of the building is computed based on the contributions of each mode of vibration (Eq. (1)) [29].

$$m_{eq} = \Gamma_i \cdot m \cdot \phi_i \tag{1}$$

where ϕ_i and Γ_i are the natural vibration mode and the modal participation factor of the ith mode, respectively. Parameter m represents the mass matrix of the building assumed as a lumped-mass system. All modes having a modal contribution greater than 5 % in the considered

5

108   direction have been considered. Furthermore, the equivalent damping c_{eq} is evaluated according

109   to the Rayleigh formulation by assuming the two predominant frequencies and setting a 5%

110   damping ratio.

111   The capacity of each building is simulated through a four-linear and a tri-linear backbone curves

112   for RC and masonry buildings, respectively. The first ones have been assumed for RC buildings

113   to better capture the gradually degrading stiffness that starts from the yield point up to perfectly

114   plastic response. The hysteretic behavior is reproduced by Takeda, Sozen [30] model adopting

115   the unloading slope k_u equal to the elastic loading k_y (Fig. 1b).

2.1 Capacity model for RC frame building

117   A four-linear backbone curve is assumed to reproduce the global seismic response (Fig. 2) where

118   V_b is the base shear and u_{top} the top displacement. The first point of the backbone curve (1)

119   indicates the yield point which refers to the formation of the first plastic hinge in the weakest

120   column. Then, the global stiffness decreases until the weakest column reaches its maximum

121   capacity (2). The frame is then subjected to a massive distribution of the internal actions that are

122   described by a further stiffness decrease. The maximum global capacity is reached at point (3),

123   from where the structure is subjected to a plastic mechanism until collapse (4).
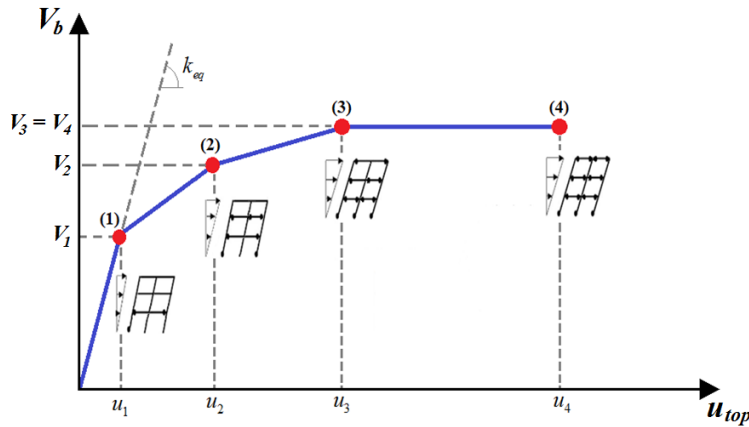

124

125   Fig. 2. Proposed four-linear backbone curve, representative of the global capacity of RC
126   buildings

2.1.1 Computation of point (1): elastic parameters

128   The RC building is modeled as a bending type MDOF system with lumped masses. Different

129   methods can be employed to include modal effects in pushover analysis [31], such as those

130   specified in FEMA 356 [32] for a first-mode dominant response, or in Chopra and Goel [29] for

131   Modal Pushover Analysis (MPA). Kunnath [33] proposed a modal combination procedure that

132   involves appropriate modes. Therefore, the lateral force F_i applied at the ith floor related to j^{th}

133   mode is computed as follows (Eq. (2)):

134
$$F_i = \sum_{j=1}^{dof} \pm \alpha_j \cdot \Gamma_j \cdot m \cdot \phi_{ij} \cdot S_{a,j}(\zeta_j, T_j) \tag{2}$$

135   The factor α_j is a modification factor that controls the relative effects of jth mode, Γ_j and ϕ_j are

136   the jth modal participation factor and modal shape, respectively. Parameter m is the total mass,

137   while $S_{a,j}$ represents the maximum spectral acceleration of the corresponding mode.

138   Following Kunnath [33], a method of the weighted average of the individual mode is herein

139   proposed, while the modification factor and the direction of the mode are neglected. These

140   simplifications lead to consider a number of modes n_d less than dof (Eq. (3)).

141
$$\Phi_{eq} = \sum_{i=1}^{n_d} \Gamma_i \cdot \{\Phi_i\} \tag{3}$$

142   Furthermore, the horizontal load pattern is considered to be proportional to the elastic story

143   forces (Eq. (4)) by α coefficient that is monotonically increased to perform the pushover

144   analysis.

145
$$\{F\} = \alpha [K_R] \{\Phi_{eq}\} \tag{4}$$

146   where *[K_R]* represents the stiffness matrix by Guyan [34]. The yielding point (u_1, V_1) is identified

147   when the maximum allowable internal stress is reached in the most stressed column.

148   ***2.1.2 Post-elastic parameters (Points (2), (3), and (4))***

149   In the following, the post-elastic behavior of the backbone curve is presented through an inverse

150   approach.

151   *Maximum shear capacity (V_4)*

152   The maximum shear capacity ($V_3=V_4$; Fig. 2) is estimated through the kinematic theorem of limit

153   analysis that requires the evaluation of different collapse mechanisms [35]. In the proposed

154   methodology, three elementary failure mechanisms are considered: *floor, beam*, and *multistory*

155   mechanisms [35]. The floor mechanism is identified by plastic hinges formation at the top and

156   bottom of the columns at a certain story level, while the multistory mechanism consists of a

157   global collapse mechanism. When the collapse mechanism is due to the formation of plastic

158   hinges at the beam-joints and within its span, a beam mechanism occurs. The collapse multiplier

159   (λ) is evaluated by imposing the equivalence of the external virtual work and the internal one

160   considering the generation of elementary collapse mechanisms and on their linear combination

161   [36].

162   Given the yield capacity of each structural member, the collapse multiplier associated with the

163   three selected elementary mechanisms is resumed in Fig. 3. The parameter *i* refers to the ith story,

164   while *j* identifies the jth weakest story where plastic hinges form. $M_{c,y,i}$ and $M_{b,y,i}$ are the yield

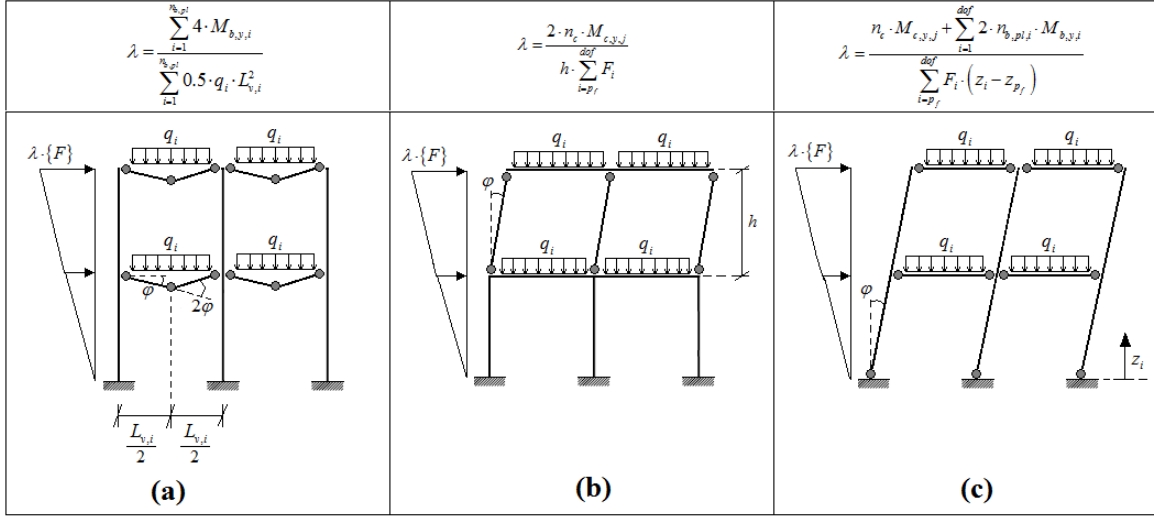165   moments of the ith story columns and beams, respectively.

The table at the top of the figure contains three collapse multiplier expressions:

$$\lambda = \frac{\sum_{i=1}^{n_{b,pl}} 4 \cdot M_{b,y,i}}{\sum_{i=1}^{n_{b,pl}} 0.5 \cdot q_i \cdot L_{v,i}^2}$$

$$\lambda = \frac{2 \cdot n_c \cdot M_{c,y,j}}{h \cdot \sum_{i=p_f}^{dof} F_i}$$

$$\lambda = \frac{n_c \cdot M_{c,y,j} + \sum_{i=1}^{dof} 2 \cdot n_{b,pl,i} \cdot M_{b,y,i}}{\sum_{i=p_f}^{dof} F_i \cdot \left(z_i - z_{p_f}\right)}$$

(a)   (b)   (c)

Fig. 3. Beam (a) floor (b) and multistory (c) collapse mechanism and associated collapse multiplier of a RC building

Coefficients n_c and $n_{b,pl,i}$ (Fig. 3) represent the number of plastic hinges in the columns and beams for the ith story level, respectively, while φ is the plastic rotation. The minimum collapse multiplier is selected among the combination of elementary collapse mechanisms and the maximum shear capacity is given as follow

$$V_3 = V_4 = \lambda \cdot V_1 \tag{5}$$

Ultimate collapse displacement (u_4)

The ultimate displacement capacity (u_4) is evaluated through the geometrical model in Fig. 4. The related mathematical expression is given in Eq. (6).

$$u_4 = \Delta_1 + \Delta_2 + \Delta_3 = \theta_u \cdot h_j + H_e \cdot \left(\theta_u - \frac{F_j \cdot h_j^2}{3 \cdot E_j \cdot I_j} \right) + \{\phi_{eq}\} \cdot u_1 \tag{6}$$

where Δ_1 represents the top column displacement due to the formation of the plastic hinge at the base of the weakest column, while Δ_2 is the horizontal displacement at the top of the building due to the rotation on the top of the weakest column (Fig. 4). The top displacement (Δ_3) represents the elastic contribution that is proportional to the equivalent modal shape multiplied by the yield

9

182   top displacement. Index j refers to the weakest story level, H_e is the effective building height

183   (from the weakest level to the top of the building), while θ_u is the ultimate chord rotation

184   estimated according to [37] (Eq. (7)):

185    $$\theta_u = \varphi_y \cdot \frac{L_v}{3} + (\chi_u - \chi_y) \cdot L_{pl} \cdot \left(1 - \frac{0.5 \cdot L_{pl}}{L_v}\right) \tag{7}$$

186   where φ_y represents the yield rotation of the weakest column, L_v is the shear length of the

187   weakest column which is assumed to be equal to half column length. The length of the plastic

188   hinge (L_{pl}) is fixed as 10 % of the shear length, while χ_u and χ_y identify the ultimate and yield
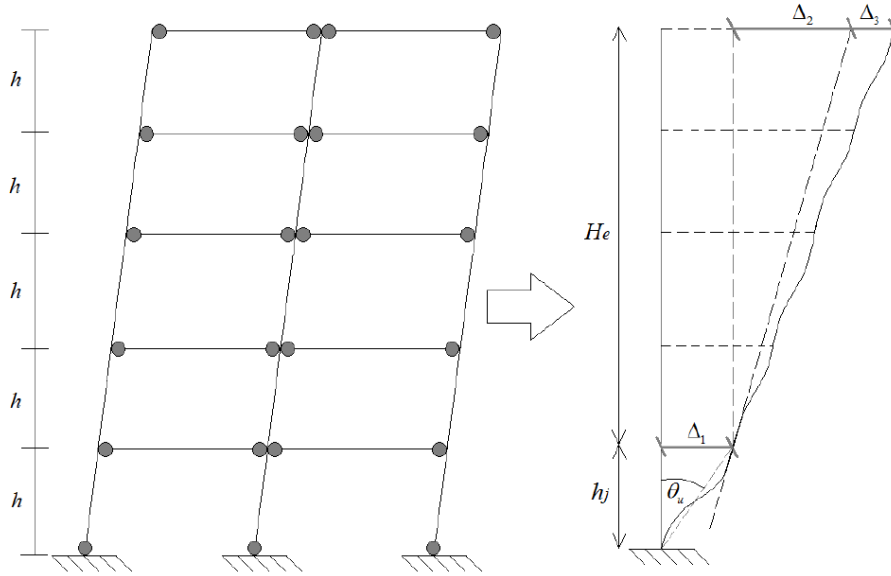
189   curvature of the weakest column.

190
191   Fig. 4. Simplified geometrical model used to estimate the collapse top displacement of RC

192   building

193   *Shear capacity corresponding to Point 2 (V_2)*

194   As depicted in Fig. 5, the base shear V_2 is identified as the intersection of the line CC' and the

195   capacity curve and can be computed following Eq. (8).

196    $$V_2 = c_2 \cdot \lambda \cdot V_{b,y} \tag{8}$$

10

197   where c_2 is derived by performing sensitivity analysis considering 220 RC Moment Resisting

198   Frames (MRF), designed according to general capacity design rules [37] (two, four, six, eight

199   and ten stories; two, four, six, and eight spans; Fig. 6). Their span length has been fixed to 5.50

200   m and the story height to 3.00 m. The effect of reinforcement percentage (ρ) on the global shear

201   capacity has been investigated by assuming two categories: low ($\rho<=2\%$) and medium-high

202   reinforcement rate ($\rho>2\%$). The models have been developed using SAP2000 [38].
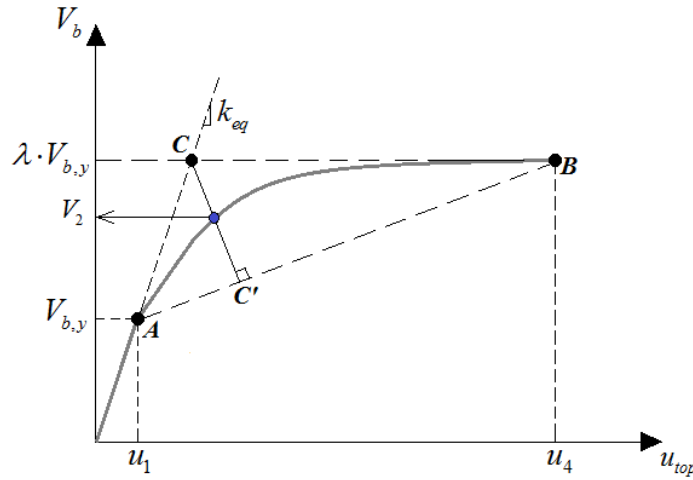
203

204   Fig. 5. Geometrical scheme for Point (2) base shear computation
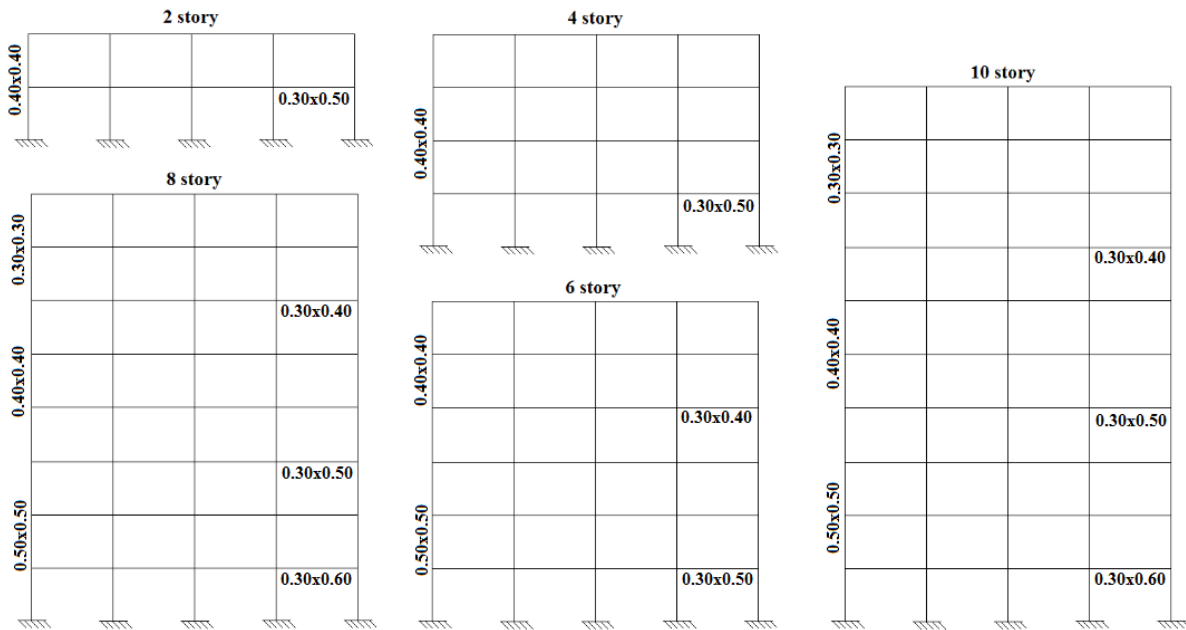
205

206   Fig. 6. Representative 2D frames considered in the sensitivity analysis

11

207 Masses have been uniformly distributed on each floor and 5% Rayleigh damping has been

208 considered. Concentrated plasticity model (FEMA 356 type P-M2-M3 for columns and beams),

209 has been chosen to take into account the nonlinearity in the structural components. The analysis

210 has been performed by monotonically increasing forces proportional to the equivalent mode, and

211 considering P–Δ effects. Finally, Eq. (9) allows estimating c_2 coefficient.

212
$$c_2 = 0.0154 \cdot n_{st} - 0.0039 \cdot n_{sp} + 0.925 - \left(1 - 0.968^{\rho_d}\right) \tag{9}$$

213 where n_{st} and n_{sp} are the number of stories and spans, respectively, while ρ_d is a dummy variable

214 that assumes zero value for low reinforcement rate and 1 for medium and high reinforcement

215 rate. Fig. 7 shows the results of the sensitivity analysis and the measure of goodness fit in terms
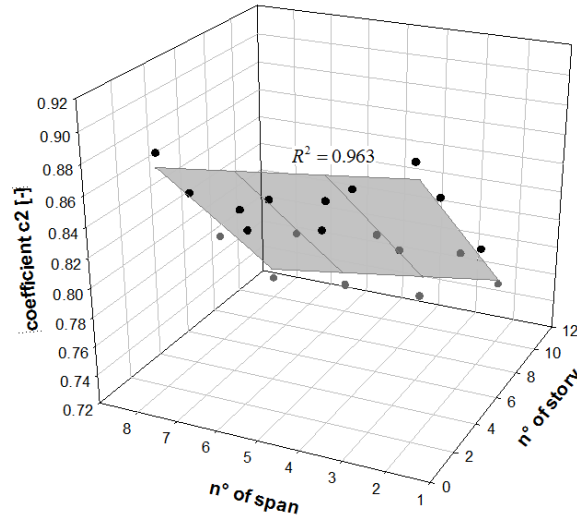
216 of the coefficient of determination (R^2).

217
218 Fig. 7. Goodness fit measure of Eq. (9)

219 *Top displacements corresponding to the Point 2 and 3 (u_2,u_3)*

220 Displacements u_2 and u_3 are estimated using the equal energy rule and assuming line through

221 Points (2) and (3) is parallel to that one through Points (1) and (4) (Fig. 8). Therefore, the

222 equivalent elastic energy ($A_{055'}$) is equal to the elasto-plastic energy ($A_{012344'}$).
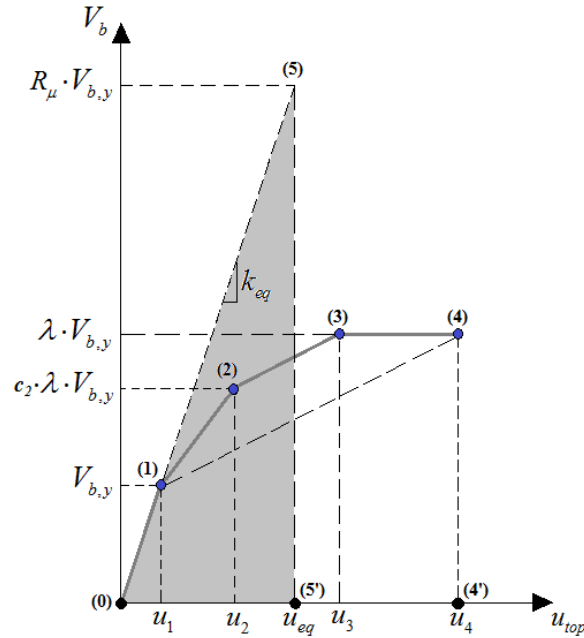
223
Fig. 8. Illustrative scheme of the physical assumptions

225 Following the second assumption, u_3 is given by Eq. (10).

$$u_3 = u_2 + \frac{u_4 - u_1}{V_{b,y} \cdot (\lambda - 1)} \cdot \lambda \cdot V_{b,y} \cdot (1 - c_2) \qquad (10)$$

227 Moreover, equal energy rule is expressed by Eq. (11).

$$\frac{\left(R_\mu \cdot V_{b,y}\right) \cdot u_{eq}}{2} = V_{b,y} \cdot \left[\lambda \cdot u_4 + \lambda \cdot u_3 \cdot \left(\frac{c_2 - 1}{2}\right) + u_2 \cdot \left(\frac{1 - 3 \cdot c_2 \cdot \lambda}{2}\right) - u_1 \cdot \frac{c_2 \cdot \lambda}{2} \right] \qquad (11)$$

229 where R_μ is the reduction factor that is a function of the unknowns u_2 and u_3, while u_{eq} is the

230 elastic displacement associated with Point (5). Finally, u_2 and u_3 are evaluated by the following

231 iterative procedure:

232 - Step 1: A value of the reduction factor is fixed;

233 - Step 2: Eq. (10) is substituted in Eq. (11) and u_2 is calculated;

234 - Step 3: u_3 is assessed through Eq. (10);

235 - Step 4: The following conditions have to be verified (Eq. (12)):

13

236
$$u_3 < u_4 \quad \text{and} \quad u_2 > \frac{c_2 \cdot \lambda \cdot V_{b,y}}{k_{eq}} \tag{12}$$

237 - Step 5: If previous conditions are verified, the reduction factor is saved. Otherwise, the

238   procedure from Step 1 to Step 4 has to be repeated.

239 Among all the obtained values of reduction factor, the mean values ($R_{\mu,mean}$) is adopted, and u_2

240 and u_3, associated with $R_{\mu,mean}$, are evaluated.

2.2 Capacity model for masonry buildings

242 Masonry buildings are classified as Un-Reinforced Masonry (URM) and Reinforced Masonry

243 (RM). Under seismic actions, a masonry panel is simultaneously subjected to in-plane shear and

244 out-of-plane bending [39] that can lead to different collapse mechanisms. It is common practice

245 to consider only in-plane mechanisms in the global analysis of masonry structures since the out-

246 of-plane mechanisms usually involve parts of the structure that does not affect significantly the

247 global response [40].

248 A simplified methodology based on the Equivalent Frame Model (EFM) is used to reproduce the

249 seismic response of both URM and RM buildings. Panels are idealized as frames composed of

250 deformable vertical (piers) and horizontal (spandrels) elements connected through rigid nodes.

251 Piers are the main resisting elements that carry vertical and horizontal loads, while spandrels

252 affect the boundary conditions of the piers. *Strong spandrels-weak piers model* and *weak*

253 *spandrels-strong piers model* can be adopted for seismic analysis. The nonlinear seismic

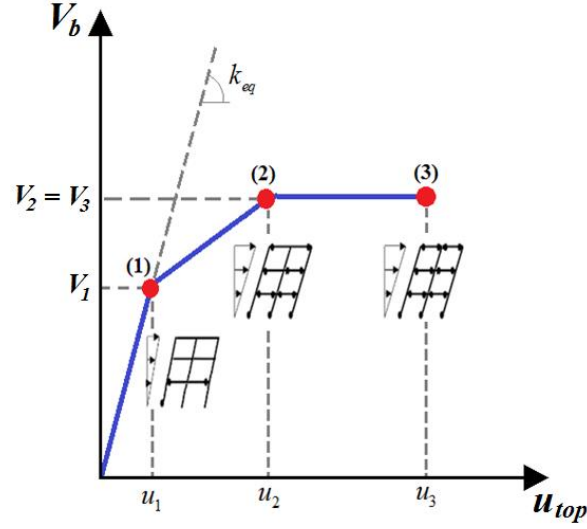254 response is simulated through the tri-linear backbone curve in Fig. 9, similarly to the RC frame

255 model.

257   Fig. 9. Proposed tri-linear backbone curve of the global capacity of masonry buildings

258   ***2.2.1 Elastic parameters at Point (1)***

259   A uniform and regular distribution of the openings on the panel is assumed, which is reasonable

260   with typical Italian masonry housing stock [41]. A coupled shear-flexure behavior is considered

261   for the piers, and the related equivalent lateral stiffness ($k_{i,h}$) is derived by Eq. (13).

262
$$k_{ih} = \frac{1}{h_i^3 / (3 \cdot E_i \cdot I_i) + 1.2 \cdot h_i / (G_i \cdot A_i)} \tag{13}$$

263   where E_i and G_i represent the longitudinal and shear elastic modulus, respectively. The principal

264   moment of inertia is expressed by I_i, whereas A_i is the cross-section area of the pier, while h_i

265   refers to the effective height of the pier, according to Dolce [42]. The multimodal approach used

266   to assess the global yield parameters of the RC buildings is adopted also for the masonry

267   building.

268   Different failure mechanisms are proposed in the literature to model the piers and spandrels

269   behavior. A shear failure with diagonal cracks (i), horizontal sliding (ii), and a rocking failure

270   (iii) are herein assumed. Force-deformation relationships (Fig. 10) to model the elastic and

271   plastic behavior are considered for the shear-based and the rocking-based mechanisms.
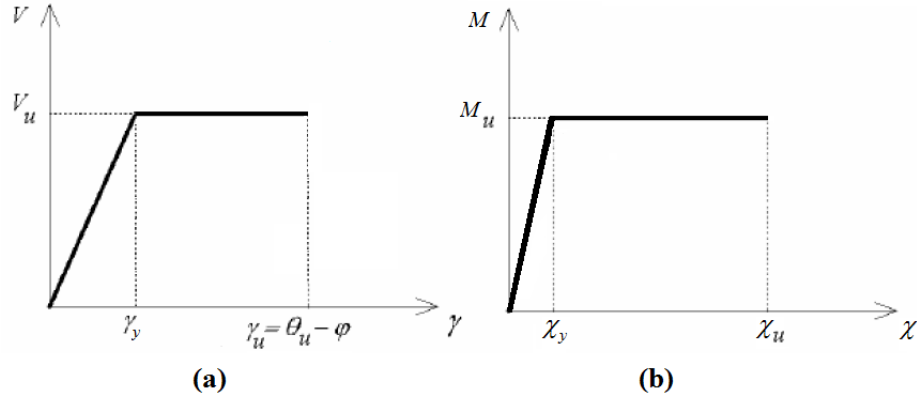
15

Fig. 10. Shear (a) and rocking (b) behavior of masonry elements

M_u and V_u represent the maximum flexural and shear (diagonal and horizontal) resistance of masonry elements, respectively. Bending moment capacity is assessed according to the Italian standard [37] which takes into account the interaction between bending moment and axial load. Diagonal shear capacity is estimated using the model proposed by [43], while the Mohr-Coloumb failure criterion is adopted to evaluate the horizontal shear capacity.

The shear capacity of the spandrels depends on the model used to simulate the piers-spandrels behavior. The model proposed by Rizzano, Sabatino [44] is assumed to include the influence of the spandrels on the global seismic behavior. Assuming weak spandrels model, the maximum shear capacity can be inferred by imposing local equilibrium, while for strong spandrels model the element is assumed as a rigid body. Depending on the piers-spandrels interaction model and the verified failure mechanism, the maximum capacity of each masonry element is estimated (Fig. 11).

16

	Maximum Bending capacity	Maximum Shear capacity	
		Diagonal shear	Sliding shear
Pier	$M_u = \left(\dfrac{\sigma_m \cdot t \cdot D^2}{2}\right) \cdot \left(1 - \dfrac{\sigma_m}{0.85 \cdot f_m}\right)$	$V_u = \dfrac{f_{td} \cdot t \cdot D}{\beta} \cdot \sqrt{1 + \dfrac{\sigma_m}{f_{td}}}$	$V_u = D_c \cdot t \cdot \left(\tau_k + 0.4 \cdot \sigma_{mc}\right)$
	(NTC08, 2008)	(Turnsek et al., 1971)	(Mohr-Coloumb)
Weak spandrel	$M_u = \left(\dfrac{f_{hd} \cdot t \cdot D^2}{2}\right) \cdot \left(1 - \dfrac{f_{hd}}{0.85 \cdot f_{hk}}\right)$	$V_u = 2 \cdot \dfrac{M_u}{l_z}$	—
	(NTC08, 2008)	(Local equilibrium)	

Fig. 11. Mathematical expression adopted to assess the shear and bending moment resistance both for piers and "weak" spandrels

Variable σ_m is the ultimate axial load ratio that is given by the ratio between the ultimate compression load (N_u) and the cross-section area of the pier; f_{hd} represents the ratio between the ultimate horizontal compression load (N_{uh}) and the cross-section area of the pier; f_m and f_{hk} represent the compression strength and the horizontal compression strength, respectively. The diagonal shear strength is represented by f_{td}, while the coefficient β is assumed equal to 1.5 for slender piers ($\lambda_p \geq 1.5$) and 1 for rigid piers ($\lambda_p < 1.5$). The sliding shear capacity of the pier is proportional to the equivalent compression zone of the pier (D_c) and the sliding shear strength, which is given by the sum of the characteristic shear strength (τ_k) and 40% of the axial load ratio (σ_{mc}).

2.2.2 Post-elastic parameters (Points (2), and (3))

In the following, the post-elastic behavior of the backbone curve is presented through an inverse approach.

Maximum shear capacity ($V_2 = V_3$)

The maximum shear capacity ($V_2 = V_3$ in Fig. 9) is estimated through the kinematic theorem of limit analysis. Different elementary in-plane collapse mechanisms can be identified considering

17

304   the pier-spandrel interaction model and on the formation of flexural or shear plastic hinges (Fig.

305   12).

306   The index i represents the ith story level and j identifies the jth weakest story where the plastic

307   hinge forms. Accordingly, $M_{pu,i}$ and $M_{su,i}$ are the ultimate moments, while $V_{pu,i}$ and $V_{su,i}$ the

308   ultimate shear forces. The denominators in Fig. 12 refers to the external work due to the

309   horizontal force distribution, while n_p and $n_{s,pl,i}$ represent the number of plasticized piers and

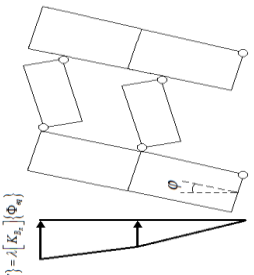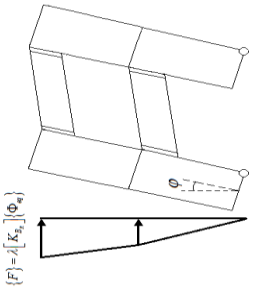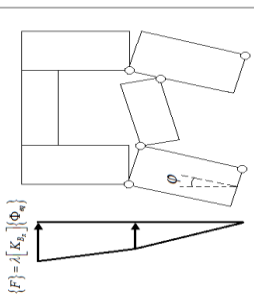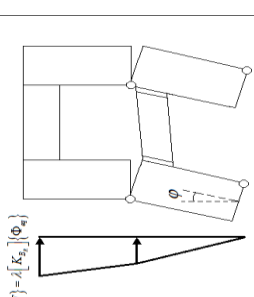310   spandrels for the ith story level.
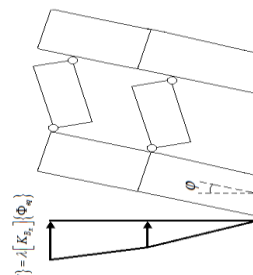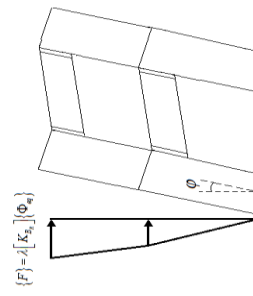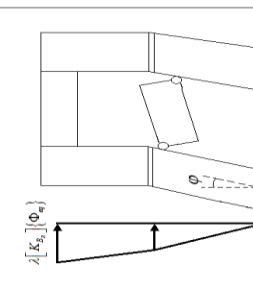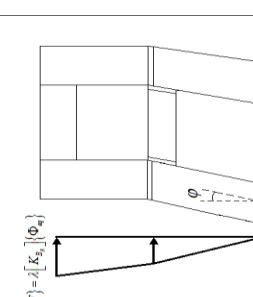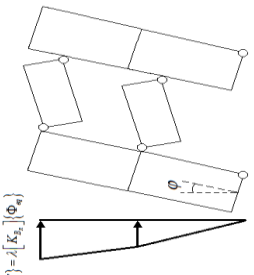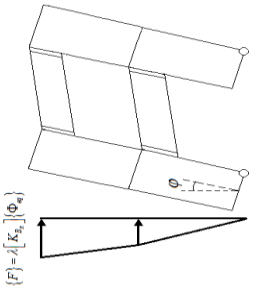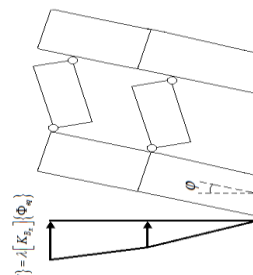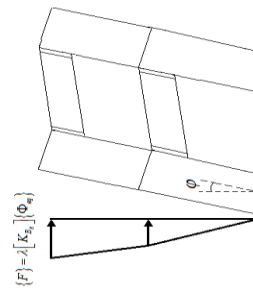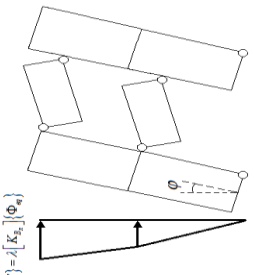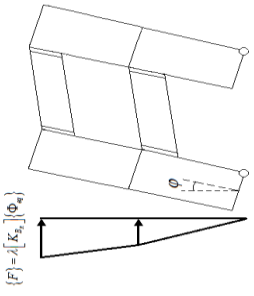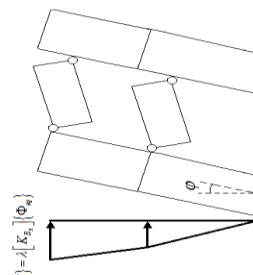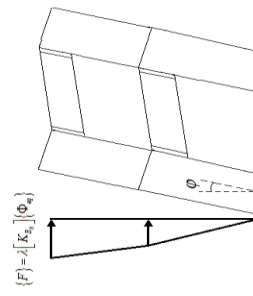
SPANDREL

	Bending failure	Shear failure		

$\{F_i\} = \lambda[K_{B_i}]\{\Phi_{eq}\}$

$\lambda = \dfrac{n_p \cdot M_{Pu,j} + \sum\limits_{i=1}^{def} 2 \cdot n_{sp,i} \cdot M_{Su,y,i}}{\sum\limits_{i=1}^{def} F_i \cdot (z_i - z_{pl})}$

GLOBAL MECHANISM (strong pier-weak spandrel)

$\{F_i\} = \lambda[K_{B_i}]\{\Phi_{eq}\}$

$\lambda = \dfrac{n_p \cdot M_{Pu,j} + \sum\limits_{i=1}^{def} n_{sp,i} \cdot V_{Su,y,i} \cdot l_i}{\sum\limits_{i=1}^{def} F_i \cdot (z_i - z_{pl})}$

$\{F_i\} = \lambda[K_{B_i}]\{\Phi_{eq}\}$

$\lambda = \dfrac{0.5 \cdot n_p \cdot V_{Pu,j} \cdot l_i + \sum\limits_{i=1}^{def} 2 \cdot n_{sp,i} \cdot M_{Su,y,i}}{\sum\limits_{i=1}^{def} F_i \cdot (z_i - z_{pl})}$

$\{F_i\} = \lambda[K_{B_i}]\{\Phi_{eq}\}$

$\lambda = \dfrac{0.5 \cdot n_p \cdot V_{Pu,j} \cdot l_i + \sum\limits_{i=1}^{def} n_{sp,i} \cdot V_{Su,y,i} \cdot l_i}{\sum\limits_{i=1}^{def} F_i \cdot (z_i - z_{pl})}$

LOCAL MECHANISM (strong pier-weak spandrel)

Bending failure

$\lambda[K_{B_i}]\{\Phi_{eq}\}$

$\lambda = \dfrac{2 \cdot n_p \cdot M_{Pu,j} + 2 \cdot n_{sp,i} \cdot M_{Su,y,i}}{h \cdot \sum\limits_{i=1}^{def} F_i}$

$\lambda = \dfrac{n_p \cdot V_{Pu,j} \cdot l_i + 2 \cdot n_{sp,i} \cdot M_{Su,y,i}}{h \cdot \sum\limits_{i=1}^{def} F_i}$

Shear failure

$\{F_i\} = \lambda[K_{B_i}]\{\Phi_{eq}\}$

$\lambda = \dfrac{2 \cdot n_p \cdot M_{Pu,j} + n_{sp,i} \cdot V_{Su,y,i} \cdot l_i}{h \cdot \sum\limits_{i=1}^{def} F_i}$

$\{F_i\} = \lambda[K_{B_i}]\{\Phi_{eq}\}$

$\lambda = \dfrac{n_p \cdot V_{Pu,j} \cdot l_i + n_{sp,i} \cdot V_{Su,y,i} \cdot l_i}{h \cdot \sum\limits_{i=1}^{def} F_i}$

LOCAL MECHANISM (weak pier-strong spandrel)

$\{F_i\} = \lambda[K_{B_i}]\{\Phi_{eq}\}$

$\lambda = \dfrac{2 \cdot n_p \cdot M_{Pu,j}}{h \cdot \sum\limits_{i=1}^{def} F_i}$

$\{F_i\} = \lambda[K_{B_i}]\{\Phi_{eq}\}$

$\lambda = \dfrac{n_p \cdot V_{Pu,j} \cdot l_i}{h \cdot \sum\limits_{i=1}^{def} F_i}$

Bending failure **Shear failure**

PIER

311
312   Fig. 12. Possible collapse mechanisms for weak spandrels-strong pier and weak pier-strong
313   spandrels model considering shear and flexural plastic hinges and associated collapse multipliers

314   *Ultimate collapse displacement (u₃)*

315   The geometrical model proposed for RC building (Fig. 4) is used to evaluate u_3. The ultimate

316   chord rotation values are assumed 0.6% in case of rocking failure and 0.4% in the case of shear

317   failure [45].

318   *Top displacement corresponding to the extensive damage (u₂)*

319   The iterative procedure used for RC building is herein adopted to evaluate u_2 following the equal

320   energy rule.

321   **2.3 Modeling uncertainties**

322   Most of the structural parameters are random, and consequently, uncertainties exist in the

323   behavior of the structural members [46]. Backbone curves are herein estimated assuming each

324   parameter as normally distributed Random Variable (RVs). Furthermore, the correlation between

325   variables is considered through multivariate normal distributions.

326   The year of construction is an essential property of each building. It affects the definition of

327   certain structural, nonstructural, and geometrical parameters. In the proposed computational

328   framework, each normally distributed building attribute is defined through a mean (μ) and a

329   standard deviation (σ) based on the year of construction. The mean building attributes are

330   assigned based on the values proposed by the design codes for a given year of construction,

331   while the standard deviations reflect the lack of knowledge in the definition of the building's

332   attributes. Based on that, the standard deviation values increase with the building's age.

333   Monte Carlo Simulations (MCS) are first performed to provide a probabilistic estimate of

334   building behavior. Then a lognormal distribution is adopted to estimate structural capacity. The

335   number of MCS iterations (n_{STEP}) is fixed when a stable estimate of the distribution parameters

336   (median θ_i and dispersion β_i) is verified (Fig. 13). The median backbone curve representative of

337   the global seismic response of individual building is characterized by the envelope of the median

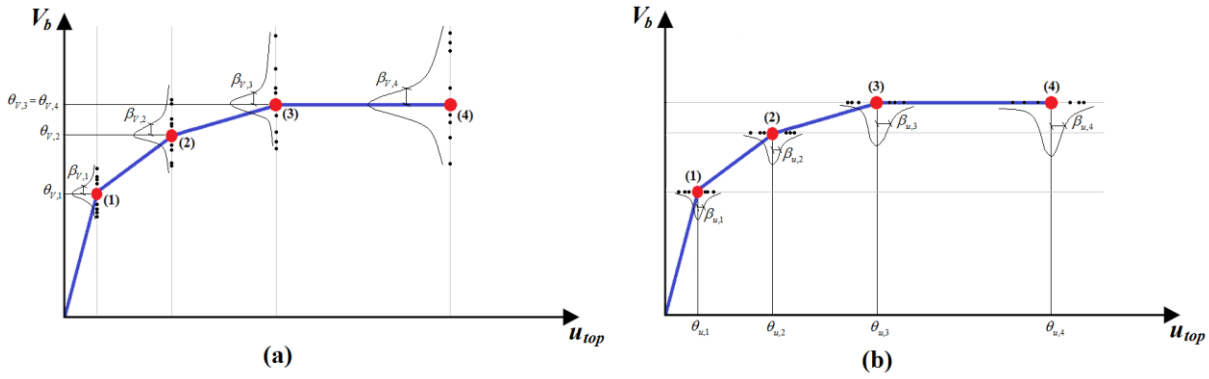338   pairs of base shear and top displacement values.

339
340   Fig. 13. Dispersions associated with the base shear (a) and top displacements (b) for an RC

341   building

342 **3. DAMAGE ASSESSMENT**

343 Following HAZUS [47], seismic damage is herein established on deformation criteria and can be

344 classified in five Damage States (DSs): *none*, *slight*, *moderate*, *extensive*, and *complete damage*,

345 with respect to different inter-story drift levels. To identify the inter-story drift associated to each

346 DS the approach proposed by Ghobarah [48] has been considered, where both RC concrete and

347 masonry buildings are classified into ductile and non-ductile systems according to their energy

348 dissipation capacity.

349 Nonlinear time-history analyses are performed by modeling for each buildings adopting the

350 surrogated model, using the median backbone curve and the hysteresis law in both horizontal

351 directions. Besides, equivalent damping is evaluated according to Rayleigh formulation, while

352 equivalent mass is concentrated on the top of the systems.

353   Maximum absolute top displacement is a global indicator; therefore it is not representative of the

354   damage experienced at each story level. On the contrary, according to ATC‑58 [49], the inter-

355   story drift ratio can be considered as a reasonable parameter to predict seismic performance.

356   To convert maximum absolute top displacements to maximum inter-story drifts, a simplified

357   approach is herein adopted. The lateral displacement distribution of individual buildings is

358   evaluated as the sum of elastic (u_e) and plastic (u_p) contributions (Fig. 14).
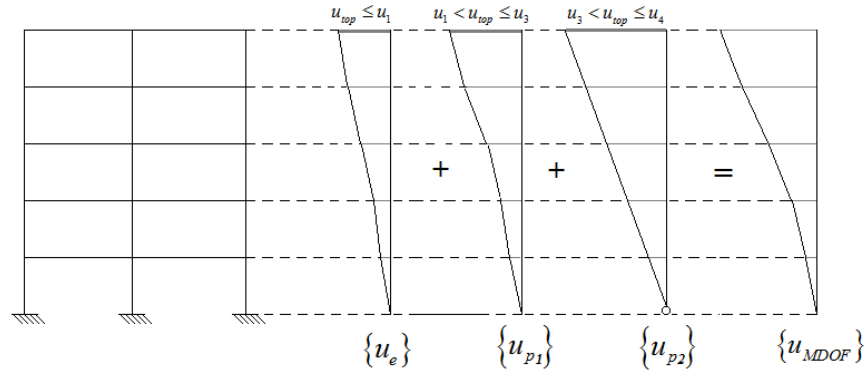

359
360   Fig. 14. Elastic and plastic lateral displacement distributions

361   The first contribution u_e is proportional to the equivalent modal shape. The plastic contribution in

362   turn is split into u_{p1} and u_{p2}. For sake of simplicity, the first part of the plastic horizontal

363   displacements is assumed to be proportional to the equivalent modal shape magnified by the ratio

364   between the initial stiffness k_e and the degraded stiffness connected to the second and the third

365   part of the backbone curve.

366   The second part u_{p2} is associated with the collapse mechanism. Thus, the lateral displacement

367   distribution is assumed as directly proportional to the collapse displacement distribution. Fig. 15

368   resumes the mathematical formulation of the proposed simplified model. Finally, maximum

369   inter-story drifts are compared with the threshold values of the inter-story drifts proposed by

370   Ghobarah [48] to assess the damage level.

	RC	Masonry
$u_{top} \leq u_1$	$\{u\} = \{\phi_{eq}\} \cdot u_{top}$	$\{u\} = \{\phi_{eq}\} \cdot u_{top}$
$u_1 < u_{top} \leq u_2$	$\{u\} = \{\phi_{eq}\} \cdot \left[u_1 + (u_{top} - u_1) \cdot \dfrac{(u_2 - u_1)}{u_1 \cdot (c_2 \cdot \lambda - 1)} \right]$	$\{u\} = \{\phi_{eq}\} \cdot \left[u_1 + (u_{top} - u_1) \cdot \dfrac{(u_2 - u_1)}{u_1 \cdot (\lambda - 1)} \right]$
$u_2 < u_{top} \leq u_3$	$\{u\} = \{\phi_{eq}\} \cdot \left[u_1 + \dfrac{(u_2 - u_1)^2}{u_1 \cdot (\lambda \cdot c_2 - 1)} + (u_{top} - u_2) \cdot \dfrac{(u_3 - u_2)}{u_1 \cdot \lambda \cdot (1 - c_2)} \right]$	$\{u\} = \{\phi_{eq}\} \cdot \left[u_1 + \dfrac{(u_2 - u_1)^2}{u_1 \cdot (\lambda - 1)} \right] + \{\phi_p\} \cdot (u_{top} - u_2)$
$u_3 < u_{top} \leq u_4$	$\{u\} = \{\phi_{eq}\} \cdot \left[u_1 + \dfrac{(u_2 - u_1)^2}{u_1 \cdot (\lambda \cdot c_2 - 1)} + \dfrac{(u_3 - u_2)^2}{u_1 \cdot \lambda \cdot (1 - c_2)} \right] + \{\phi_p\} \cdot (u_{top} - u_3)$	——

Fig. 15 Mathematical formulations to obtain the lateral displacement distribution

4. VALIDATION OF THE SURROGATED MODEL

Three different case studies have been considered to numerically validate the proposed computational framework [38]. The first and second case studies are a five and seven-story RC building with a square and rectangular planar layout, respectively. The third case study is a four-story unreinforced brick masonry building.

The selected case studies have been used to firstly compare the proposed surrogated model with FE-based results. Subsequently, the surrogated model is compared with two existing approaches that are: (*i*) RISK-UE LM2 [22], and (*ii*) nonlinear shear MDOF model proposed by Lu and Guan [19].

The first case study has been designed to meet the requirements of capacity design rules and to reproduce the global collapse mechanism. On the contrary, the second case study has been designed to have a soft-story mechanism, by drastically reducing columns stiffness at the fourth story level. Both buildings have a span length of 4.40 m in the *x*-direction and 6.00 m in *y*-direction, whereas a story height of 3.00 m is used. The structural members have been designed according to the Italian seismic regulations [37], while the columns are tapered in elevation as shown in Fig. 16.a and Fig. 16.b. A two-ways floor system has been modeled for the two RC frames, while a rigid deck behavior is assumed by releasing both horizontal displacements and

390   the rotation around the vertical axis only. To cope with the reduced flexibility of the frame joints,

391   the rigid links have been adopted by assuming the overlapped beam-column zones as infinitely

392   rigid. A symmetric reinforcement has been adopted for columns and beams in both horizontal

393   directions. A strength class C 30/37 characterizes concrete material, while the B450C strength

394   class has been considered for the steel reinforcements. Steel reinforcement ratios of 2.5 % and

395   1.8 % have been adopted for columns and beams, respectively. Concentrated plasticity model

396   (FEMA 356 type P-M2-M3 for columns and M2-M3 for beams) has been chosen to take into

397   account the nonlinearity in the structural components. Takeda model has been selected for

398   hysteresis behavior. A 5% damping ratio has been assumed according to Rayleigh formulation.

399   The third case study is a four-story unreinforced brick masonry building studied as Equivalent

400   Frame. The walls' thickness is assumed of 0.30 m, while openings have dimensions of 1.30×2.00

401   m. The masonry building has a story height of 4.00 m. The effective length of the piers equals to

402   3.24 m has been evaluated according to Dolce [42]. The deformable length of spandrels is 2.65

403   m, while the width of its cross-section is equal to 0.76 m. A compression strength of 9.40 MPa, a

404   Young modulus of 94000 MPa, and a shear elastic modulus of 37600 MPA have been selected.

405   Shear and flexural plastic hinges have been set based on elastic perfectly plastic force-

406   deformation relationships [38]. Fig. 16 illustrates the 3D models and their structural
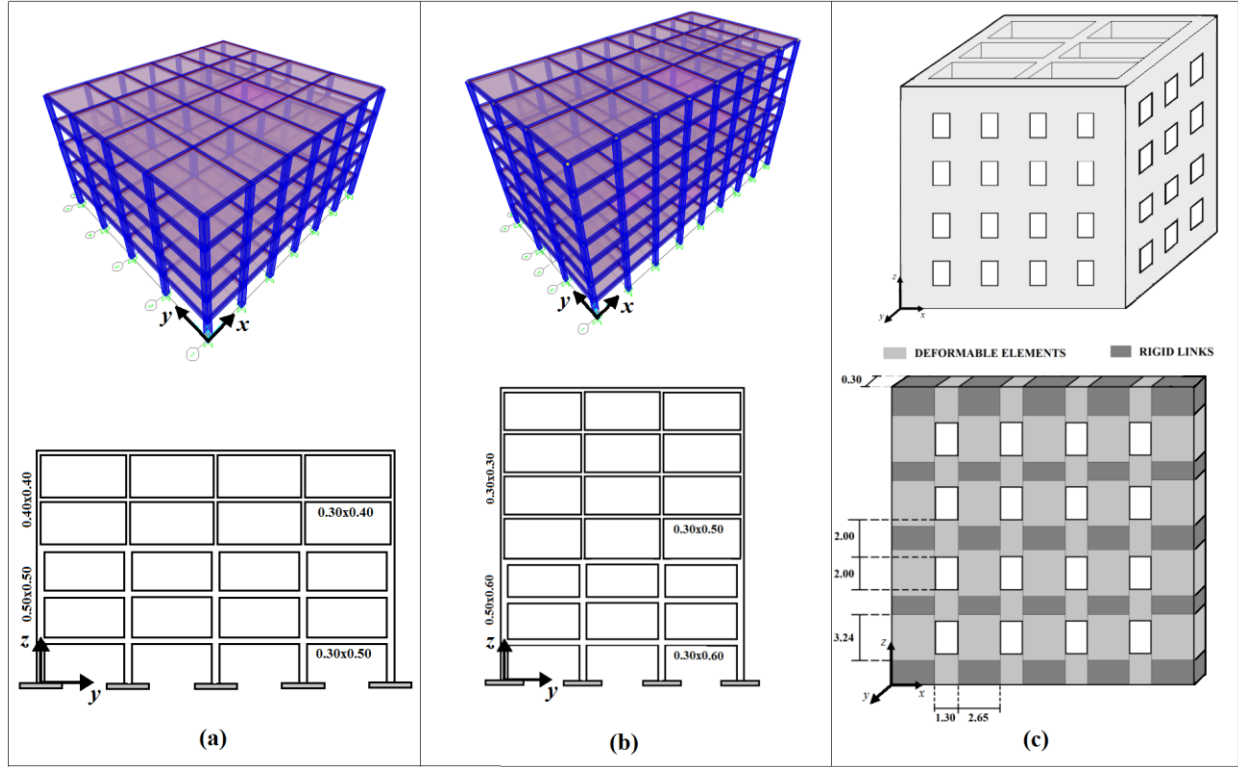
407   configuration.

Fig. 16. 3D models and configurations of the first (a), second (b), and third (c) case studies

The comparison between the surrogated and the FE models has been conducted in terms of (i) capacity curves and (ii) dynamic response. Moreover, the capacity curves have been also compared with existing methods (RISK-UE LM2 [22], Lu and Guan [19]).

For the three multi-story case studies, the lateral force distributions proportional to the equivalent modal shape have been considered and nonlinear pushover analyses have been performed in both horizontal directions. The material and mechanical parameters have been considered as RVs using their mean values μ_{mat} and μ_{mec} for both surrogated and FE models. The standard deviations associated with the mechanical (σ_{mec}) and material (σ_{mat}) parameters have been set to 0.2 μ_{mec} and 0.15 μ_{mat}, respectively [49]. MCSs have been performed with 100 iterative steps, and the median backbone curves have been assessed for both horizontal directions.

To assess the dynamic analysis, the El Centro seismic record has been used as input ground motion [50]. A PGA of 0.61 g has been adopted to clearly show the elastic-plastic response of

25

422   the Finite Element (FE) models and then compare the results obtained through the proposed

423   surrogated model. The comparisons have been carried out in terms of dynamic displacement

424   response of the top center of the mass of the building in both horizontal directions. Finally,

425   comparisons in terms of maximum inter-story drift are also presented.

426   **4.1 Results**

427   A satisfactory comparison between the capacity curves is shown in Fig. 17. For the second case

428   study, the maximum shear capacity assessed by the proposed methodology is slightly lower than

429   the expected value (Fig. 17b) in both directions. Indeed, because of the soft-story mechanism, the

430   simplified methodology tends to underestimate the collapse multiplier and consequently the

431   maximum shear capacity. Similar considerations are also found for the capacity curve associated

432   with the third case study (Fig. 17c). For the first two case studies, results confirm that

433   considering a four-linear backbone curve increases the accuracy in describing the stiffness

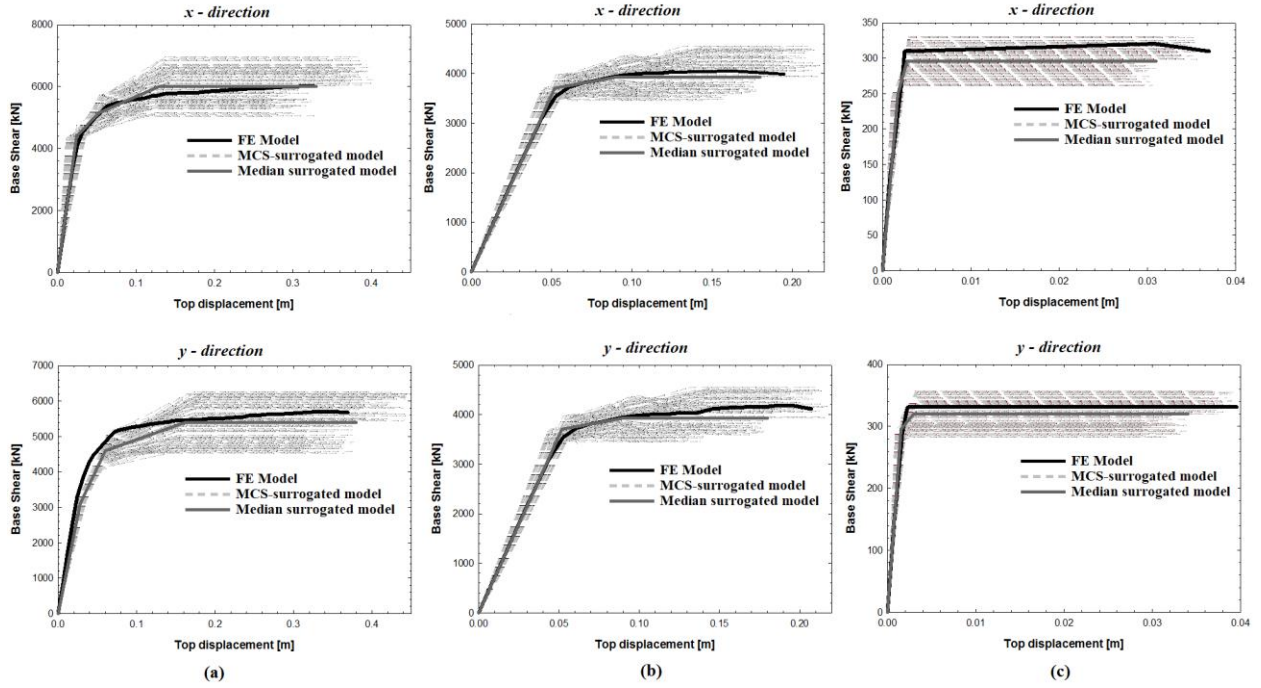434   degradation beyond the yield point.

435

Fig. 17. Comparison between the capacity curves of FE model and estimated backbone curve derived by using the proposed surrogated model for the first (a), second (b), and third (c) case study building in both horizontal directions

Table 1 reports the median and dispersions values of base shear (ϑ_{Vi}, β_{Vi}) and roof displacements (ϑ_{ui}, β_{ui}) for the first case study building running MCS. Furthermore, the correlation coefficients ($\rho_{Vi\text{-}ui}$) have been calculated and statistical independency verified.

Table 1. Mean and dispersion associated with the base shear and top displacement characteristic values for the first case study building and related correlation coefficients

	θ		β/θ		ρ
	V [kN]	u [m]	V	u	
Point 1	4405	0.022	0.040	0.051	-0.001
Point 2	5219	0.045	0.156	0.142	0.009
Point 3	6056	0.119	0.245	0.190	0.006
Point 4	6350	0.279	0.222	0.271	-0.069

Comparisons of the dynamic response in terms of top displacement are depicted in Fig. 18. For the first case study, the results show a satisfactory accuracy of the surrogated model in predicting both the dynamic response and residual deformation. For the second and third case studies, due

27

448   to the soft-story mechanism, some differences have been captured when plastic deformations

449   occur (Fig. 18b and Fig. 18c).

450   (a)   (b)   (c)
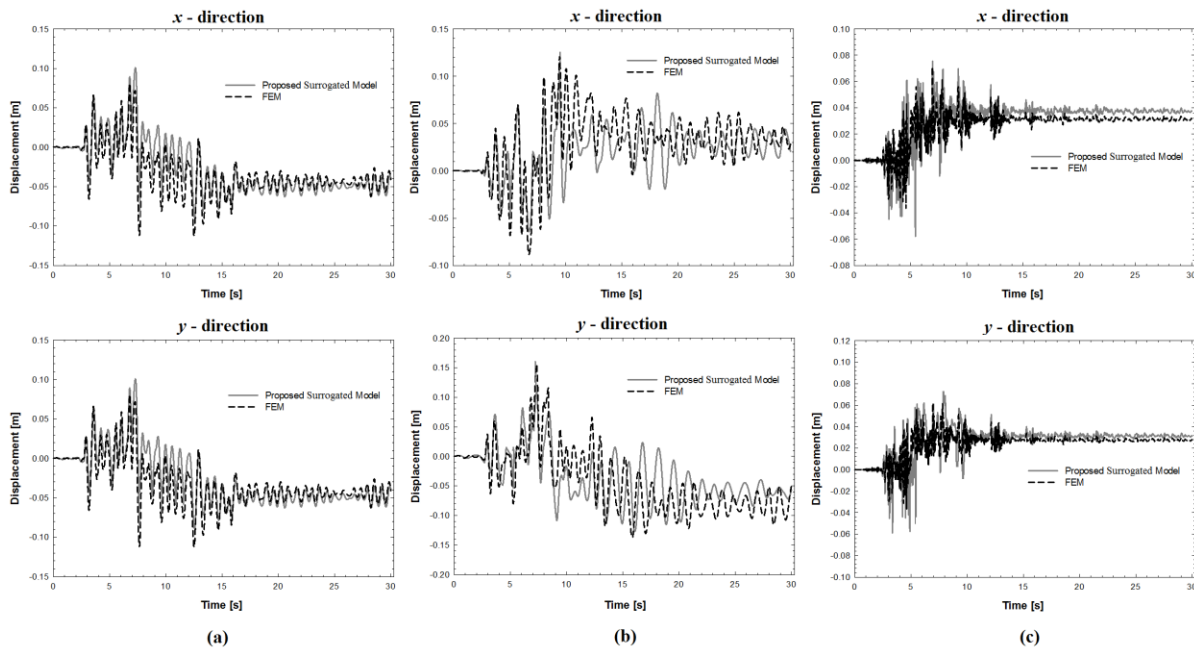
451   Fig. 18. Comparison of the dynamic response in term of top displacements for the first (a),

452   second (b), and third (c) case study building in both horizontal directions

453   An additional satisfactory comparison has been provided in Fig. 19 to verify the hysteresis

454   behavior.

455
456   Fig. 19. Comparison of the hysteretic loop for the first case study building between the FE model

457   and proposed model

458   Maximum inter-story drifts are evaluated for both the surrogated and FE model and presented in

459   Table 2. The error in evaluating the maximum drift ratio results in the range of 0-9 %.

460 Table 2. Maximum inter-story drifts assessed through the proposed surrogated and FE models

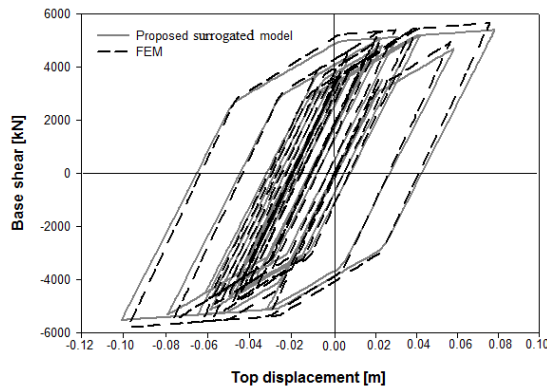|	Direction	FE model	Proposed model	Error [%]
Case study 1	X	0.92	1.01	9.78
	Y	0.94	0.88	-6.38
Case study 2	X	1.57	1.58	0.64
	Y	3.02	2.87	-4.97
Case study 3	X	1.79	1.90	6.15
	Y	1.63	1.75	7.36

461

462 **4.2 Comparisons with existing methods**

463 The capacity curves of the three case studies have been computed by using the RISK-UE LM2

464 method [22] and the approach proposed by Lu and Guan [19]. The first method aims at

465 identifying a bilinear capacity curve, while the second one is based on the definition of a tri-

466 linear backbone curve.

467 RISK-UE method defines the yield shear as a function of the design strength coefficient and the

468 overstrength factor that relates the design strength to the real yield strength. The displacement

469 associated with the yield point is determined based on the first period of vibration. Therefore, the

470 ultimate shear and displacement are determined based on the overstrength and ductility factors.

471 All the aforementioned coefficients are related to standard requirements. EC8 provisions [51] are

472 herein adopted to determine the parameters which allow to evaluate the bilinear capacity curve.

473 Lu and Guan [19] proposed an MDOF lumped mass model where the seismic response is

474 dominated by the inter-story shear deformation. A tri-linear backbone curve is adopted to

475 simulate the capacity of the building where the characteristics parameters are determined based

476 on the Chinese design codes and the statistical data obtained from the experimental and

477 analytical studies.

478 The capacity curve of the two considered existing approaches are computed by assuming the

479 same mean values of the geometrical, mechanical, and construction attributes adopted for the

480   surrogated model. Fig. 20 illustrates the comparisons among different approaches of the capacity

481   curves for the three case study buildings in both horizontal directions. For RISK-UE LM2 model,

482   the first case study corresponds to Mid-rise Reinforced Concrete Moment Frame (RC1M), the

483   second case study corresponds to High-rise Reinforced Concrete Moment Frame (RC1H), while

484   the third case study corresponds to Mid-rise Unreinforced masonry Simple Stone (M12M).

485
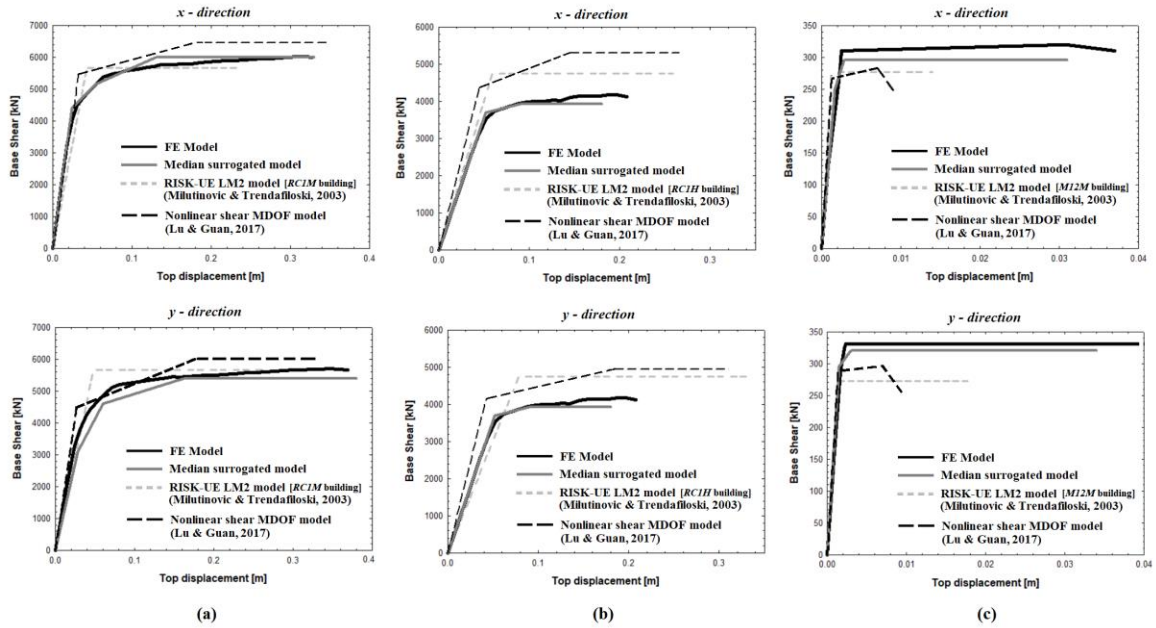
486   Fig. 20. Comparison between the capacity curves of FE model, proposed surrogated model,

487   RISK-UE LM2 model [22], and Lu and Guan [19] model for the first (a), second (b), and third

488   (c) case study building in both horizontal directions

489

490   All the capacity curves obtained for the first case study building shows comparable results in

491   terms of both shear forces and displacements (Fig. 20.a). This can be justified by the building

492   regularity both in plan and elevation that ensure the conformity of the design parameters.

493   Furthermore, the use of a four-linear back-bone curve for the surrogated model leads to

494   accurately model the post-yield characteristics of the capacity curve, while the two considered

495   methods (RISK-UE LM2 [22] and Lu and Guan [19]) do not provide consistent capacity

496   estimates.

497   Considering the second case study, the two approaches (RISK-UE LM2 [22] and Lu and Guan

498   [19]) provide an overestimation of the building strength and ductility, while the proposed

499   surrogated model is consistent with the FE-based capacity curve. These discrepancies are caused

500   by the stiffness irregularity of the building leading to a local collapse mechanism. Indeed, the

501   design requirements adopted to evaluate the post-elastic coefficients for RISK-UE LM2 [22] and

502   Lu and Guan [19] models are essentially based on regular structure, leading to overestimate the

503   shear capacity and the ultimate collapse displacement (Fig. 20.b).

504   Finally, the capacity curves associated to the third case study and computed with RISK-UE LM2

505   [22] and Lu and Guan [19] models show an underestimation of the ultimate deformation and

506   shear capacity (Fig. 20.c). Therefore, they tend to model the post-elastic masonry behavior with

507   low ductile capacity, with respect to the proposed surrogated model.

508   **5. COMPARISON WITH REAL POST-EARTHQUAKE SCENARIO**

509   In this section, comparison of the proposed surrogated model with a real post-earthquake

510   scenario is provided for validation. It consists of damage data of downtown of the Municipality

511   of Norcia after the seismic event of Central Italy (6.5 Mw, 2016/10/30) [52]. The building stock

512   is composed of 719 buildings including 95% masonry and 5% RC buildings from one to four

513   story levels. About 56% of the buildings were built before 1919, while most of them have been

514   retrofitted after the seismic events of 1971, 1979, and 1997. The building stock is classified

515   based on their structural configuration, geometry, quality of the members, and retrofitting

516   actions.

517   Post-earthquake damage data has been collected through the survey conducted by Italian Civil

518   Protection. Accordingly, buildings have been classified as unsafe, partially unsafe, temporary

519   unsafe, and safe. This classification is based on the building practicability after seismic events

520   depending on structural and nonstructural damage, and proximity with other structurally unsafe

521   buildings [53]. A building is considered unsafe or partially unsafe when the entire building or

522   part of it is significantly damaged and then life-safety is at risk. Based on this definition,

523   unsafe and partially unsafe states may be considered as equivalent to extensive damage state

524   [47]. A building is classified as temporary unsafe when limited structural damage occurs

525   without compromising life safety and it can return safely through simple rapid actions.

526   Therefore, a temporary unsafe condition is comparable with a moderate damage state.

527   Finally, safe conditions represent fully operational levels where the life risk is null, which

528   can be assumed as a slight damage state. Furthermore, partial and total buildings' collapse

529   reported in the survey are considered a complete damage state. The proposed surrogated

530   model is used to assess the damage of each single building located within the downtown

531   area. The seismic scenario has been defined through the horizontal acceleration time histories

532   of the Central Italy earthquake (6.5 Mw, 2016/10/30) recorded in the station of Norcia (NRC in

533   Fig. 22). Fig. 21 illustrates the recorded time history and the frequency content.

534
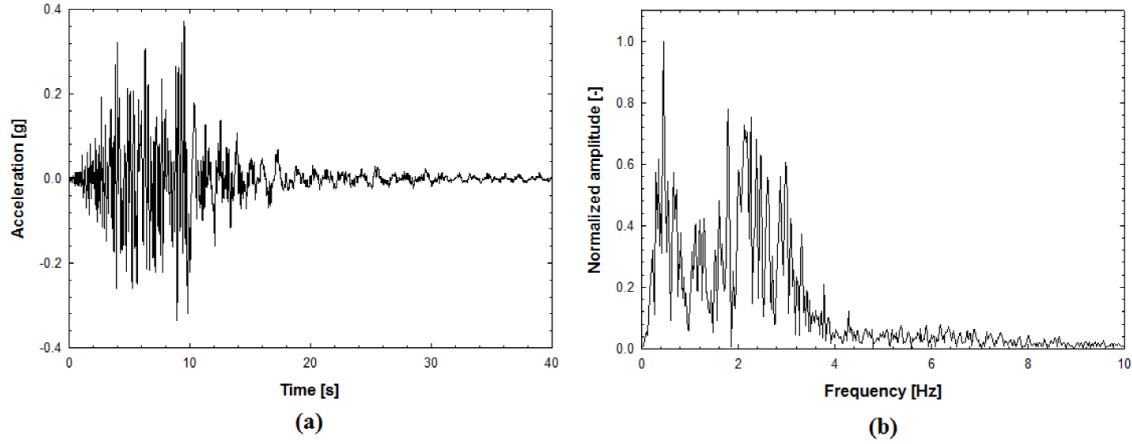
Fig. 21. (a) North-South acceleration time history recorded in the station of Norcia (NRC) during the

Central Italy earthquake, and (b) the associated frequency content

Fig. 22 depicts the comparisons between the results of the numerical simulation and the real

post-earthquake damage scenario. It can be noted satisfactory compatibility between the results,

in particular for complete and extensive DSs, while the small differences are mainly related to

different definitions of the DSs itself and the way the data were collected on-site.

541

Fig. 22. Comparison between the DSs as from the simulations (a) and real post-earthquake

scenario of Norcia (b)

544   A global goodness index has been computed to describe how well the numerical simulations fit

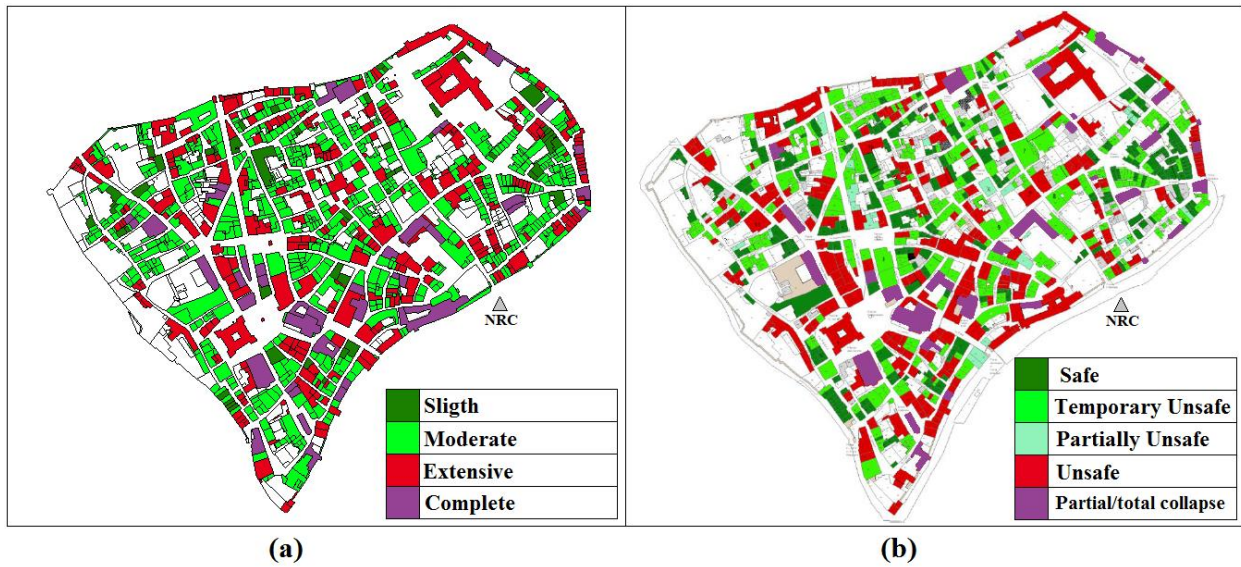545   the observations. It is estimated giving to each building a value of 1 or 0 if there is an agreement

546   between the simulated damage level and the real observations or not, respectively. Then, the

547   global goodness index is obtained summing each building's index and dividing it by the total

548   number of buildings. A measure of goodness of 83% provides a satisfactory comparison.

549   The raw post-earthquake data herein adopted are in line with the assumptions of the proposed

550   methodology. They report the experienced damage level based on a qualitative approach using a

551   rapid visual screening of each building. However, it is worth noting how the use of raw post-

552   earthquake data may lead to misleading results since the vulnerability of the building portfolio

553   depends on the mutual interactions with the surrounding buildings and infrastructures. Indeed, a

554   building could be considered unsafe even if it experienced low damage due to external causes

555   (e.g. heavy damaged surrounding building, interrupted road access).

556

557   **6. FRAMEWORK APPLICATION TO A LARGE-SCALE VIRTUAL CITY**

558   In this section, the computational framework is applied to a virtual city named "*Ideal City"[54]*

559   that consists of 23420 residential buildings. The building information such as occupancy and

560   physical characteristics of the structures (building archetype, year of construction, and height

561   classifications) have been collected for being representative of the average characteristics of the

562   housing stock of the city of Turin, Italy. The overall area of the city of Turin is around 120 km^2

563   with a population of more than 900.000 inhabitants. The building stock of the city is

564   representative of a typical Italian building portfolio. Fig. 23a illustrates the distribution of the

565   buildings based on the archetypes (37% masonry and 63% RC), while Fig. 23b shows the

566   building distribution based on the year of construction.

34

567   A simplified seismic scenario has been assumed by defining epicenter location, moment

568   magnitude, and time history recorded in the epicenter. Geometrical attenuation at any building

569   location has been estimated based on the Ambraseys model [55], adopting constant frequency

570   content between the stations (buildings). Therefore, the site amplification has been defined in

571   terms of PGA attenuation with the distance to the epicenter. The building-epicenter distances

572   have been evaluated and used in the attenuation relationship as geometrical distance parameter.

573   A stiff soil has been considered to model the ground conditions of the virtual city, where the

574   shear velocity in the uppermost 30 m ranges between 360 and 750 m/s.

575   The horizontal acceleration time histories of the Central Italy earthquake (6.5 Mw, 2016/10/30)

576   in the station of Norcia (NRC) have been adopted for the analysis (Fig. 21). Fig. 23c shows the

577   map of PGA and the epicenter location. MCSs have been performed using 30 iterations and the

578   median backbone curve has been evaluated for each building. Time history analyses have been

579   then executed and each dynamic building response has been estimated.

580   The computational procedures are performed through a Rack Server with no. 2 Intel Xeon (E5-

581   2698 v4 2.2GHz, 50M Cache, 9.60GT/s QPI, Turbo, HT, 20C/40T (135W) Max Mem

582   2400MHz) and 256 Gb RAM (8x32GB RDIMM, 2400MT/s, Dual Rank, x4 Data Width). To

583   improve the computational performance for large scale simulations, the surrogated model has

584   been implemented within OpenSees in Python [56]. The measured running time has been

585   estimated in about 16 minutes for the entire "*Ideal City*".

586   Fig. 23d depicts the map of the damage experienced by the buildings [48]. The results show that

587   downtown (*C3* in Fig. 23d) is mainly composed of old masonry buildings (see Fig. 23a) and it is the

588   most vulnerable zone. The spatial distribution of the building archetypes (see Fig. 23a) confirms that

589   vulnerability distribution is higher in the zones where the older buildings are located (Fig. 23b) since

590   they were not designed according to updated seismic design requirements. The results confirm that

591   the damage is mostly experienced by masonry buildings rather than RC ones.
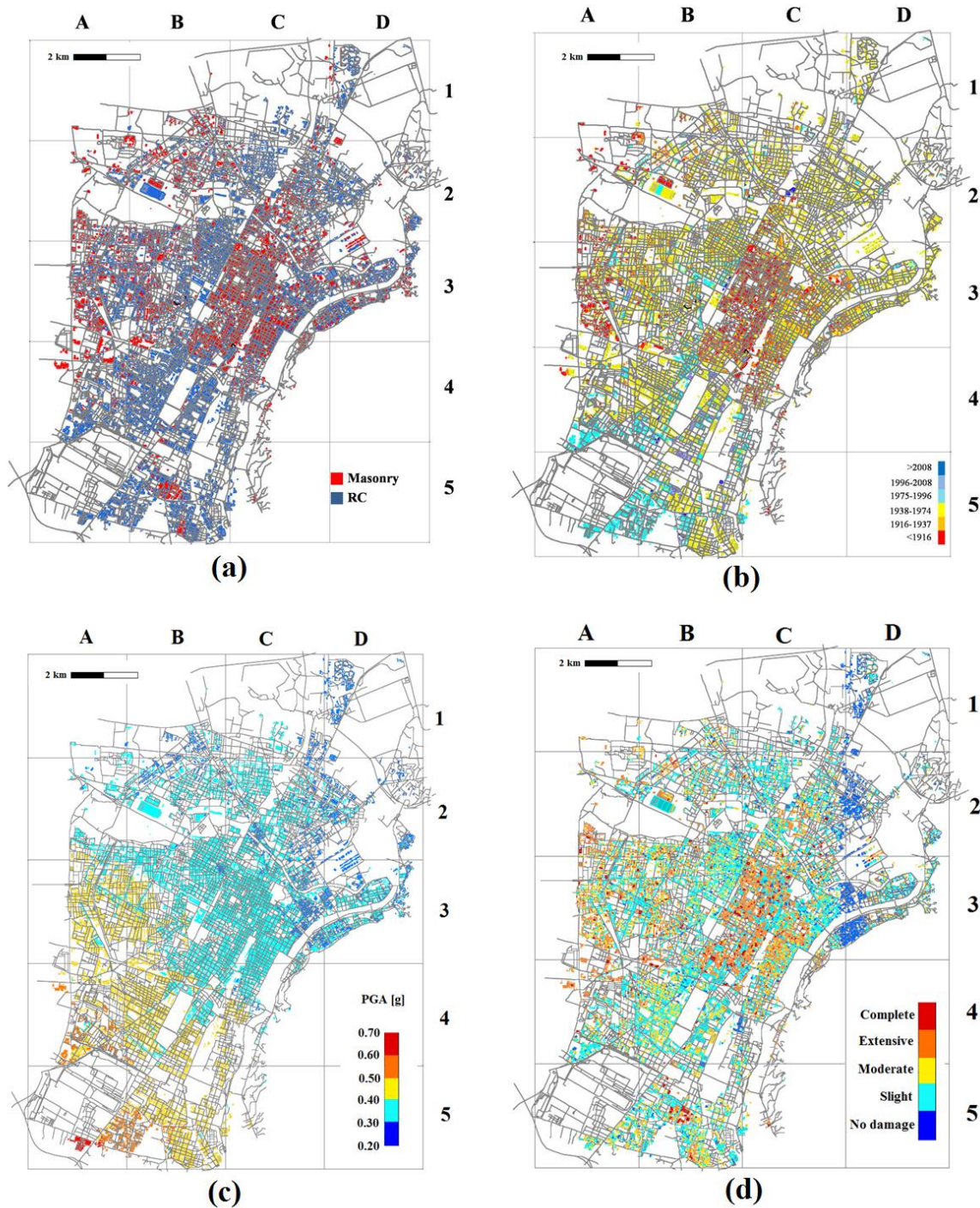
592

(a)

(b)

(c)

(d)

593

594   Fig. 23. Distribution of buildings within "Ideal City" based on building archetype (a), year of
595   construction (b), seismic excitation in terms of PGA (c), and level of damage (d). The star
596   indicates the epicenter location.

597   Furthermore, the total percentages of buildings associated with each DS have been calculated

598   and reported in Fig. 24a. Most of the buildings have experienced slight damage (about 38 %),

599   while 30 % and 22 % of the buildings experienced moderate and extensive damage, respectively.

600   Only 3 % of the buildings are collapsed, whereas the remaining part is undamaged (about 9 %).

601   The distribution of damaged buildings and the year of construction is shown in Fig. 24b.

602

(a)   (b)
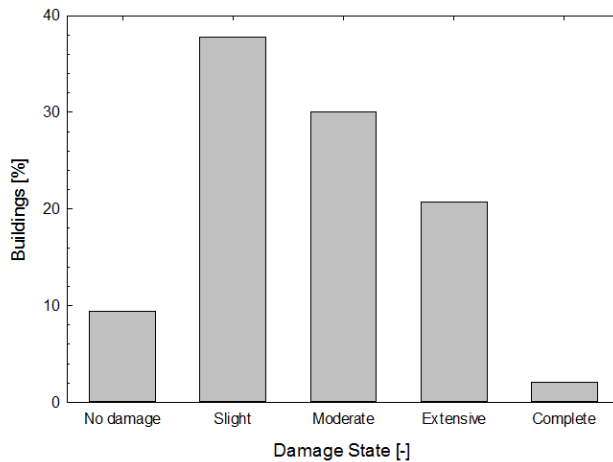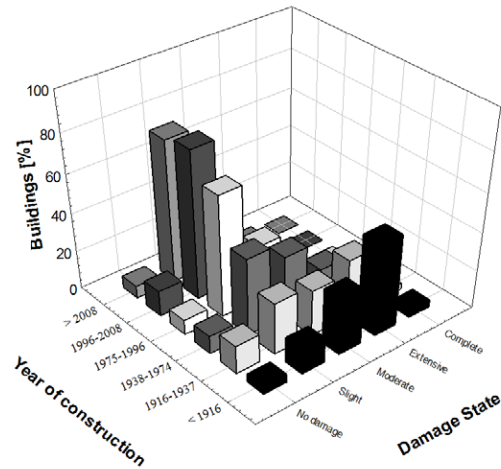
603
604   Fig. 24. Buildings' damage distribution (a) and percentage distribution based on year of
605   constructions (b) within "Ideal City".

606   Results show that most of the buildings built before 1916 (e.g., coordinates C3 in Fig. 23b) have

607   experienced extensive damage, although more distant from the epicenter, than newest buildings

608   (A5 in Fig. 23b), designed with more stringent seismic design requirements, although closer to

609   the epicenter, which show slight damage.

610   **7. CONCLUDING REMARKS**

611   The prediction of physical damage and the impact of natural hazards on the building portfolio are

612   challenging issues for community developers and decision-makers. This work is focused on the

613   numerical assessment of earthquakes impact on urban areas. The seismic capacity of each

614   building has been estimated through a surrogated model. Uncertainties have been included by

615   using the Monte Carlo simulations. Nonlinear time-history analyses have been performed and

616   structural damage has been estimated based on the maximum inter-story drift. The proposed

617   surrogated model, suitable both for RC and masonry buildings, leads to accurately identify the

618   individual building capacity. The proposed model has been validated using a real post-

619   earthquake scenario. Then, it has been tested on a large-scale city, showing a direct

620   proportionality between the experienced damage to the buildings category and their age.

621   Moreover, masonry buildings were found to be more vulnerable than RC buildings.

622   The surrogated nonlinear model stands at an intermediate level between a detailed description of

623   the built environment and a typological one. It results in computationally effective and providing

624   an accurate estimate considering both the individual building characteristics and the inherent

625   uncertainties. The limited computational demand and the clear representation of the output

626   scenario make the surrogate model a useful tool for a rapid assessment of the damage by

627   decision-makers, even those that are not experts in the field.

634   **REFERENCES**

635   [1] Malalgoda C, Amaratunga D, Haigh R. Challenges in creating a disaster resilient built
636   environment. Procedia Economics and Finance. 2014;18:736-44.

637   [2] Cimellaro GP, Marasco S. A computer-based environment for processing and selection of
638   seismic ground motion records: OPENSIGNAL. Frontiers in Built Environment. 2015;1:17.
639   [3] Kammouh O, Zamani-Noori A, Cimellaro GP, Mahin SA. Resilience Assessment of Urban
640   Communities. ASCE-ASME Journal of Risk and Uncertainty in Engineering Systems, Part A:
641   Civil Engineering. 2019;5.
642   [4] Cimellaro, Renschler C, Reinhorn AM, Arendt L. PEOPLES: a framework for evaluating
643   resilience. Journal of Structural Engineering, ASCE. 2016;142:1-13 DOI:
644   0.1061/(ASCE)ST.943-541X.0001514.
645   [5] Cimellaro GP, Solari D, Bruneau M. Physical infrastructure Interdependency and regional
646   resilience index after the 2011 Tohoku earthquake in Japan. Earthquake Engineering &
647   Structural Dynamics. 2014;43:1763-84.
648   [6] Kammouh O, Dervishaj G, Cimellaro GP. Quantitative framework to assess resilience and
649   risk at the country level. ASCE-ASME Journal of Risk and Uncertainty in Engineering Systems,
650   Part A: Civil Engineering. 2018;4:1-14.
651   [7] Cimellaro GP, Scura G, Renschler C, Reinhorn AM, Kim H. Rapid building damage
652   assessment system using mobile phone technology Earthquake Engineering and Engineering
653   Vibration. 2014;13:519-33
654   [8] Whitman RV. Damage Probability Matrices for Prototype buildings; Seismic Design
655   Decision Analysis. Cambridge, Massachusetts: Massachusetts Institute of Technology; 1973.
656   [9] Rojahn C, Sharpe RL. Earthquake damage evaluation data for California: Applied technology
657   council; 1985.
658   [10] Dolce M, Kappos A, Masi A, Penelis G, Vona M. Vulnerability assessment and earthquake
659   damage scenarios of the building stock of Potenza (Southern Italy) using Italian and Greek
660   methodologies. Engineering Structures. 2006;28:357-71.
661   [11] Eleftheriadou AK, Karabinis AI. Evaluation of damage probability matrices from
662   observational seismic damage data. International Journal of Earthquakes and Structures. 2013;4.
663   [12] Freeman SA. Review of the development of the capacity spectrum method. ISET Journal of
664   Earthquake Technology. 2004;41:1-13.
665   [13] Fajfar P, Gašperšič P. The N2 method for the seismic damage analysis of RC buildings.
666   Earthquake Engineering & Structural Dynamics. 1996;25:31-46.
667   [14] El Ezz AA, Nollet M-J, Nastev M. Assessment of earthquake-induced damage in Quebec
668   city, Canada. International journal of disaster risk reduction. 2015;12:16-24.
669   [15] Korkmaz K. Seismic safety assessment of unreinforced masonry low-rise buildings in
670   Pakistan and its neighbourhood. Natural Hazards and Earth System Sciences. 2009;9:1021.
671   [16] Tang B, Lu X, Ye L, Shi W. Evaluation of collapse resistance of RC frame structures for
672   Chinese schools in seismic design categories B and C. Earthquake engineering and engineering
673   vibration. 2011;10:369.
674   [17] Vamvatsikos D, Cornell CA. Incremental dynamic analysis. Earthquake Engineering &
675   Structural Dynamics. 2002;31:491-514.
676   [18] Xu Z, Lu X, Guan H, Han B, Ren A. Seismic damage simulation in urban areas based on a
677   high-fidelity structural model and a physics engine. Natural hazards. 2014;71:1679-93.
678   [19] Lu X, Guan H. Earthquake disaster simulation of civil infrastructures: from tall buildings to
679   urban areas: Springer; 2017.
680   [20] Silva V, Crowley H, Pagani M, Monelli D, Pinho R. Development of the OpenQuake
681   engine, the Global Earthquake Model's open-source software for seismic risk assessment.
682   Natural Hazards. 2014;72:1409-27.

683   [21] Villar-Vega M, Silva V, Crowley H, Yepes C, Tarque N, Acevedo AB et al. Development
684   of a fragility model for the residential building stock in South America. Earthquake spectra.
685   2017;33:581-604.
686   [22] Milutinovic ZV, Trendafiloski GS. Risk-UE An advanced approach to earthquake risk
687   scenarios with applications to different european towns. Contract: EVK4-CT-2000-00014, WP4:
688   Vulnerability of Current Buildings. 2003:1-111.
689   [23] Grünthal G. European macroseismic scale 1998. European Seismological Commission
690   (ESC); 1998.
691   [24] Hori M, Ichimura T, Oguni K. Development of Integrated Earthquake Simulation for
692   estimation of strong ground motion, structural responses and human actions in urban areas.
693   2006:381-92.
694   [25] Hori M, Ichimura T, Wijerathne L, Ohtani H, Chen J, Fujita K et al. Application of high
695   performance computing to earthquake hazard and disaster estimation in urban area. Frontiers in
696   Built Environment. 2018;4:1.
697   [26] Sahin A, Sisman R, Askan A, Hori M. Development of integrated earthquake simulation
698   system for Istanbul. Earth, Planets and Space. 2016;68:115.
699   [27] Cimellaro GP, Marasco S. Methods of Analysis. Introduction to Dynamics of Structures
700   and Earthquake Engineering: Springer; 2018. p. 331-51.
701   [28] Marasco S, Zamani Noori A, Cimellaro GP. Cascading hazard analysis of a hospital
702   building. Journal of Structural Engineering. 2017;143:04017100.
703   [29] Chopra AK, Goel RK. A modal pushover analysis procedure for estimating seismic
704   demands for buildings. Earthquake engineering & structural dynamics. 2002;31:561-82.
705   [30] Takeda T, Sozen MA, Nielsen NN. Reinforced concrete response to simulated earthquakes.
706   Journal of the Structural Division. 1970;96:2557-73.
707   [31] Cimellaro GP, Giovine T, Lopez-Garcia D. Bidirectional Pushover analysis of irregular
708   structures. Journal of Structural Engineering, ASCE. 2014;140:04014059.
709   [32] FEMA. Prestandard and Commentary for the Seismic Rehabilitation of Buildings. Federal
710   Emergency Management Agency FEMA 356. Washington, DC: Building Seismic Safety
711   Council; 2000.
712   [33] Kunnath SK. Identification of modal combinations for nonlinear static analysis of building
713   structures. Computer‐Aided Civil and Infrastructure Engineering. 2004;19:246-59.
714   [34] Guyan RJ. Reduction of stiffness and mass matrices. AIAA journal. 1965;3:380-.
715   [35] Neal BG, Symonds PS. THE RAPID CALCULATION OF THE PLASTIC COLLAPSE
716   LOAD FOR A FRAMED STRUCTURE. Proceedings of the institution of civil engineers.
717   1952;1:58-71.
718   [36] Greco A, Cannizzaro F, Pluchino A. Seismic collapse prediction of frame structures by
719   means of genetic algorithms. Engineering Structures. 2017;143:152-68.
720   [37] NTC. Normativa Tecnica delle Costruzioni 2018. Progettazione Sismica. Gazzetta Ufficiale
721   della Repubblica Italiana2018.
722   [38] CSI. Integrated Finite Element Analysis and Design of Structures Basic Analysis Reference
723   Manual. Computers and Structures, Inc, Berkeley, California, USA2018.
724   [39] Maheri MR, Najafgholipour M. In-plane shear and out-of-plane bending capacity
725   interaction in brick masonry walls. 15th World Conference on Earthquake Engineering, Lisbon,
726   Portugal2012.

727 [40] Bucchi F, Arangio S, Bontempi F. Seismic Assessment of an Historical Masonry Building
728 using Nonlinear Static Analysis. 14th International Conference on Civil, Structural and
729 Environmental Engineering Computing. Sardinia, Italy2013.
730 [41] Corrado V, Ballarini I, Corgnati SP. National scientific report on the TABULA activities in
731 Italy. Politecnico di Torino; 2012.
732 [42] Dolce M. Schematizzazione e modellazione per azioni nel piano delle pareti, Corso sul
733 consolidamento degli edifici in muratura in zona sismica. Ordine degli Ingegneri, Potenza (in
734 Italian). 1989.
735 [43] Turnsek V, Cacovi F. Some Experimental Results on the Strength of Brick Masonry Walls.
736 Zavod za Raziskavo Materiala, Konstrukcij, Ljubljana, Yugoslavia. 1971.
737 [44] Rizzano G, Sabatino R, Zambrano M. L'influenza delle fasce di piano sulla resistenza di
738 pareti in muratura. 2009.
739 [45] Bolognini D, Braggio C, Magenes G, terremoti Gnpldd. Metodi semplificati per l'analisi
740 sismica non lineare di edifici in muratura: CNR-Gruppo nazionale per la difesa dai terremoti;
741 2000.
742 [46] Lee T-H, Mosalam KM. Probabilistic fiber element modeling of reinforced concrete
743 structures. Computers & structures. 2004;82:2285-99.
744 [47] FEMA. Hazus: FEMA's methodology for estimating potential losses from disasters. 2011.
745 [48] Ghobarah A. On drift limits associated with different damage levels. Performance-Based
746 Seismic Design Concepts and Implementation: Proceedings of the International Workshop, Bled,
747 Slovenia2004. p. 321-32.
748 [49] ATC‐58. Guidelines for seismic performance assessment of buildings. ATC-58 50% Draft,
749 Applied Technology Council Redwood City, CA; 2009.
750 [50] Chopra AK. Dynamics of structures: theory and applications to earthquake engineering:
751 Prentice-Hall; 2001.
752 [51] Code P. Eurocode 8: Design of structures for earthquake resistance-part 1: general rules,
753 seismic actions and rules for buildings. Brussels: European Committee for Standardization. 2005.
754 [52] Borri A, Sisti R, Prota A, Di Ludovico M, Costantini S, Barluzzi M et al. ANALISI DEL
755 DANNO DEGLI EDIFICI ORDINARI NEL CENTRO STORICO DI NORCIA A SEGUITO
756 DEL SISMA DEL 20162017.
757 [53] AeDES. Manuale per la compilazione della scheda di 1° livello di ri-levamento danno,
758 pronto intervento e agibilità per edifici ordinari nell'emergenza post-sismica Roma: Presidenza
759 del Consiglio dei Ministri. Dipartimento della Protezione Civile.; 2009.
760 [54] Cimellaro GP, Zamani-Noori A, Marasco S, Kammouh O, Domaneschi M, Mahin S. Smart
761 cities to improve resilience of communities. 2nd International Workshop on Modelling of
762 Physical, Economic and Social Systems for Resilience Assessment. Brussels, 14-16 December
763 2017: Joint Research Center in collaboration with NIST; 2017.
764 [55] Ambraseys NN, Simpson Ku, Bommer JJ. Prediction of horizontal response spectra in
765 Europe. Earthquake Engineering & Structural Dynamics. 1996;25:371-400.
766 [56] Zhu M, McKenna F, Scott MH. OpenSeesPy: Python library for the OpenSees finite
767 element framework. SoftwareX. 2018;7:6-11.
768